BNL-113401-2017-JA

# Reforming and oxidative dehydrogenation of ethane with CO2 as a soft oxidant over bimetallic catalysts

**MyatNoeZin Myint, Binhang Yan,**
**Jie Wan, Shen Zhao, and Jingguang G. Chen**

*Submitted to Journal of Catalysis*

November 2016

**Chemistry Department**

**Brookhaven National Laboratory**

**U.S. Department of Energy**
**USDOE Office of Science (SC),**
**Basic Energy Sciences (BES) (SC-22)**

Notice: This manuscript has been authored by employees of Brookhaven Science Associates, LLC under Contract No. DE- SC0012704 with the U.S. Department of Energy. The publisher by accepting the manuscript for publication acknowledges that the United States Government retains a non-exclusive, paid-up, irrevocable, world-wide license to publish or reproduce the published form of this manuscript, or allow others to do so, for United States Government purposes.

# DISCLAIMER

This report was prepared as an account of work sponsored by an agency of the United States Government. Neither the United States Government nor any agency thereof, nor any of their employees, nor any of their contractors, subcontractors, or their employees, makes any warranty, express or implied, or assumes any legal liability or responsibility for the accuracy, completeness, or any third party's use or the results of such use of any information, apparatus, product, or process disclosed, or represents that its use would not infringe privately owned rights. Reference herein to any specific commercial product, process, or service by trade name, trademark, manufacturer, or otherwise, does not necessarily constitute or imply its endorsement, recommendation, or favoring by the United States Government or any agency thereof or its contractors or subcontractors. The views and opinions of authors expressed herein do not necessarily state or reflect those of the United States Government or any agency thereof.

**Submitted to: Special Issue Catalytic $CO_2$ conversion processes to fuels and other small molecules**

**Journal of Catalysis**

**Date: Oct 1st, 2015**

# Reforming and Oxidative Dehydrogenation of Ethane with $CO_2$ as a Soft Oxidant over Bimetallic Catalysts

*MyatNoeZin Myint[1+], Binhang Yan[2+], Jie Wan[3], Shen Zhao[4], and Jingguang G. Chen[*2,5]*

[1]Department of Chemical and Biomolecular Engineering, University of Delaware, Newark, DE 19716

[2]Department of Chemistry, Brookhaven National Laboratory, Upton, NY 11973

[3]College of Materials Science and Engineering, Tsinghua University, Beijing 100084, China

[4]Department of Chemistry, University of Illinois, Urbana, IL 61801

[5]Department of Chemical Engineering, Columbia University, New York, NY 10027

+These authors contributed to the work equally and should be regarded as co-first authors

*Corresponding author

Telephone: (212) 854-6166 Fax: (212) 854-3054 Email: jgchen@columbia.edu

## Abstract

An efficient mitigation of abundantly available $CO_2$ is critical for sustainable environmental impact as well as for novel industrial applications. Using ethane, $CO_2$ can be catalytically converted into a useful feedstock (synthesis gas) and a value-added monomer (ethylene) via the dry reforming pathway through the C–C bond scission and the oxidative dehydrogenation pathway through the C–H bond scission, respectively. Results from the current flow-reactor study show that the precious metal bimetallic $CoPt/CeO_2$ catalyst undergoes the reforming reaction to produce syngas with enhanced activity and stability compared to the parent monometallic catalysts. In order to replace Pt, the activities of non-precious $CoMo/CeO_2$ and $NiMo/CeO_2$ are investigated and the results indicate that $NiMo/CeO_2$ is nearly as active as $CoPt/CeO_2$ for the reforming pathway. Furthermore, $FeNi/CeO_2$ is identified as a promising catalyst for the oxidative dehydrogenation to produce ethylene. Density functional theory (DFT) calculations are performed to further understand the different pathways of the $CoPt/CeO_2$ and $FeNi/CeO_2$ catalysts.



**Keywords: Reforming, Oxidative dehydrogenation, Synthesis gas, Ethylene, $CeO_2$ supports**

## 1. Introduction

Emission of $CO_2$, a byproduct from many industrial processes and power plants, has increased with increasing energy demand and growing population.[1] While viable utilization and mitigation of $CO_2$ are critical for sustainable environmental impact, catalytically activating $CO_2$, one of the most stable carbon-containing molecules, remains a challenge.[2,3] $CO_2$ can be activated to CO using hydrogen, via the reverse water gas shift (RWGS) reaction at relatively mild conditions.[4] To be carbon-efficient, the RWGS reaction requires inexpensive $CO_2$-free hydrogen, instead of hydrogen produced from the steam reforming of methane (SRM) that produces $CO_2$ as a byproduct. Alternatively, $CO_2$ conversion to synthesis gas or syngas (CO and $H_2$) can be achieved via dry reforming with the hydrogen-rich methane molecule (DRM). DRM is particularly attractive as it simultaneously transforms two abundant greenhouse gases into an important feedstock, syngas, which can be subsequently used in methanol and Fischer-Tropsch (FT) syntheses. Compared to SRM, DRM produces pure syngas without requiring the purification step and hence has lower operating cost.[5,6] However, DRM is highly endothermic and energy intensive due to high reaction temperatures, with most state-of-the-art DRM catalysts suffering from catalyst deactivation due to carbon deposition. For instance, Ni, the most common DRM catalyst, suffers serious deactivation.[7] Although the more expensive and scarce Pt-group metals such as Pt, Rh and Ru are more resistant to carbon deposition,[5,8] their limited availability and high cost have hindered their applications in the DRM processes.

An alternative way to convert $CO_2$ to syngas is to use ethane, the second-largest component of natural gas after methane.[9] Similar to methane reforming, dry reforming of ethane (DRE) (Equation 1) produces $H_2$/CO via

$$C_2H_{6(g)} + 2CO_{2(g)} \rightarrow 4CO_{(g)} + 3H_{2(g)} \qquad \Delta H^o_{25} = 429 \text{ kJ/mol} \qquad \Delta G^o_{25} = 273 \text{ kJ/mol} \qquad (1)$$

One significant advantage of DRE over DRM is that the former reaction reaches $\Delta G < 0$ at a temperature that is approximately 100 K lower than that of the latter and thus potentially reducing the operating cost

and catalyst deactivation.[2] Other reactions of $CO_2$ and ethane include oxidative dehydrogenation of ethane with $CO_2$ (ODEC) (Equation 2), non-oxidative dehydrogenation (Equation 3), cracking to produce methane (Equation 4) and RWGS to form water (Equation 5):

$$C_2H_{6(g)} + CO_{2(g)} \rightarrow C_2H_{4(g)} + CO_{(g)} + H_2O_{(l)} \quad \Delta H^o_{25} = 134 \text{ kJ/mol} \quad \Delta G^o_{25} = 121 \text{ kJ/mol} \quad (2)$$

$$C_2H_{6(g)} \rightarrow C_2H_{4(g)} + H_{2(g)} \quad \Delta H^o_{25} = 137 \text{ kJ/mol} \quad \Delta G^o_{25} = 101 \text{ kJ/mol} \quad (3)$$

$$C_2H_{6(g)} + 2CO_{2(g)} \rightarrow CH_{4(g)} + 3CO_{(g)} + H_2O_{(l)} \quad \Delta H^o_{25} = 180 \text{ kJ/mol} \quad \Delta G^o_{25} = 122 \text{ kJ/mol} \quad (4)$$

$$CO_{2(g)} + H_{2(g)} \rightarrow CO_{(g)} + H_2O_{(g)} \quad \Delta H^o_{25} = 41 \text{ kJ/mol} \quad \Delta G^o_{25} = 28 \text{ kJ/mol} \quad (5)$$

The ODEC reaction is an attractive method to produce ethylene, one of the most important building blocks in chemical industry used in the production of a variety of basic and intermediate products.[10,11] The ODEC reaction, where $CO_2$ acts as a soft oxidant, has potential advantages compared to using oxygen as an oxidant or the current production of ethylene from the highly energy intensive steam cracking of naphtha or ethane. Specifically, ODEC employs $CO_2$, which in excess can reduce the amount of coke formed at elevated temperature on the catalysts via the reverse Boudouard reaction ($CO_2 + C \rightarrow 2\ CO$), thereby increasing conversion and maintaining the stability of the catalysts. In contract, oxidative dehydrogenation of ethane with oxygen leads to total oxidation to produce the undesired $CO_2$ byproduct and hence results in low ethylene selectivity.[12]

While current research efforts focus heavily on DRM[1,5,13] and ODE with oxygen,[14,15] a comparative study of DRE and ODEC over bimetallic catalysts is still lacking. Some of the previously studied ODEC catalysts include $Ga_2O_3$- and Cr-based catalysts on various supports, mainly acidic supports such as $SiO_2$.[3,16] Addition of Fe, Co and Mn has been shown to increase the activity of transition metal oxides.[16,17,18] Besides supported transition metal oxides, supported metal carbide, $Mo_2C/SiO_2$, has also been studied for ODEC.[19] Despite the initial high activity, these catalysts suffer from low stability.[11,20]

The primary objective of the current study is to identify low-cost and stable catalysts for both DRE and ODEC, using precious and non-precious bimetallic catalysts supported on $CeO_2$. Specifically, the catalytic performance of $CoPt/CeO_2$, previously reported as a selective catalyst for $CO_2$ activation by hydrogen,[4] is evaluated against its respective monometallic catalysts, $Pt/CeO_2$ and $Co/CeO_2$, for the

reaction of $CO_2$ and ethane. In order to replace Pt, several non-precious bimetallic catalysts, $CoMo/CeO_2$, $NiMo/CeO_2$ and $FeNi/CeO_2$, are selected for parallel catalytic performance evaluation. Reducible $CeO_2$ oxide, known for its ability to promote active metal dispersion and to shift easily between reduced and oxidized states which help accommodate $CO_2$ dissociation,[21] is used as the oxide support in this work. Our results indicate that $CoPt/CeO_2$ and $NiMo/CeO_2$ are active catalysts for DRE pathway to produce syngas, while $FeNi/CeO_2$ shows promising selectivity for the ODEC pathway to produce ethylene. The experimental results are supported by DFT calculations of energetics for the DRE and ODEC pathways over CoPt and FeNi surfaces, respectively.

## 2. Materials and Methods

### 2.1 Catalyst Preparation

Monometallic (Pt, Co, Mo, Ni, and Fe) and bimetallic catalysts were synthesized by incipient wetness impregnation over as-is commercially obtained $CeO_2$ (35–45 $m^2/g$, cubic, Sigma–Aldrich) supports, as described previously.[4] Precursor solutions were prepared by dissolving $Pt(NH_3)_4(NO_3)_2$ (Alfa Aesar), $Co(NO_3)_2.6H_2O$ (Alfa Aesar), $H_{24}Mo_7N_6O_{24}.4H_2O$ (Alfa Aesar), $Ni(NO_3)_2.6H_2O$ (Alfa Aesar) and $Fe(NO_3)_3.9H_2O$ (Alfa Aesar). The catalysts were then dried at 353 K for 2–3 h and calcined at 563 K for 2 h. For all bimetallic catalysts, a co-impregnation synthesis procedure was used to maximize the number of bimetallic bond formation.[22] Metal loading amounts (atomic ratio of 1:3 for Pt:Co, Mo:Ni, Mo:Co, Ni:Fe) and calcination temperature were selected to be consistent with the previous studies from our research group.[4]

### 2.2 Catalyst Characterization

#### 2.2.1 Pulse CO Chemisorption

Using an AMI-300ip (Altamira), pulse CO chemisorption was performed to compare the number of active sites in each supported catalyst. Approximately 200 mg of catalyst was added into a U-shaped quartz tube and dried at 393 K for 30 min, under helium with a constant flow rate of 50 mL/min. The reduction was performed with a heating rate of 10 K/min from 323 K to 723 K and held at 723 K for 45 min, using a mixture of 10% $H_2$ in Ar (30 mL/min). Before pulse CO chemisorption experiments, the reduced

catalyst was purged in He (50 mL/min) at 723 K for 20 min for degassing and then cooled down to 313 K. A thermal conductivity detector (TCD) was used to analyze the amount of CO flowing out of the reactor. Pulses of 10% CO in He (loop 590 μl) were injected onto a He stream (50 mL/min) until the peak area became constant. The amount of CO adsorbed by each catalyst provides a means to calculate the turnover frequency (TOF) and quantitatively compare the activity between each supported catalyst.

**2.2.2 Temperature Programmed Reduction (TPR)**

Temperature programmed reduction (TPR) was carried out in the same AMI-300ip (Altamira) instrument equipped with a thermal conductivity detector (TCD). For each TPR experiment, approximately 200 mg of fresh catalyst was added into a U-shaped quartz tube and pre-treated at 393 K for 30 mins in a He flow (30 mL/min) and then cooled to 323 K. The flow was then switched to a mixture of 10% $H_2$ in Ar with a constant flow rate of 30 mL/min and the TPR measurements were performed with a heating rate of 10 K/min to 723 K. The amount of hydrogen consumed as a function of reduction temperature was continuously monitored and recorded by TCD, which can be used to compare the reducibility of active metals in supported catalysts and to examine the alloy formation of the bimetallic catalysts.

**2.2.3 Flow Reactor Studies**

Reactions of $CO_2$ and ethane were performed in a ¼ inch quartz reactor under atmospheric pressure. Approximately 100 mg of catalysts, sieved to 16-20 mesh, were used for steady-state experiments. Catalysts were reduced at 723 K for 1 h with a feed ratio of unity for $H_2$ and He (20 mL/min each). With the constant total flow rate at 40 mL/min, $CO_2$, $C_2H_6$ and He as a diluent were introduced at 1:1:2 ratio, respectively, into the reactor. The catalysts were heated to 873 K and kept at this temperature for 12 h for steady-state measurements. Gas products were analyzed on-line using a gas chromatography (GC), equipped with a flame ionization detector (FID) and thermal conductivity detector (TCD). Control experiments were performed using a blank quartz reactor with and without the $CeO_2$ support at 873 K. Both cases show little activity, indicating that the gas-phase reaction, quartz sand and the support will not strongly affect the reaction.

For catalysts which show a selective dehydrogenation activity, the amount of $H_2$ produced were below the detection limits of GC and therefore to be consistent, conversion, selectivity and TOF were defined as

$$Conversion = \frac{moles_{reactant}^{inlet} - moles_{reactamt}^{outlet}}{moles_{reactant}^{inlet}} \times 100\ \%$$

$$Selectivity_i = \frac{moles\ of\ carbon - containing\ product_i}{Sum\ of\ carbon - containing\ products} \times 100\ \%$$

$$TOF = \frac{Conversion \times Inlet\ Flow\ Rate \times Pressure}{CO\ Uptake \times Catalyst\ Weight \times Temperature \times R}$$

**2.3 Density Functional Theory (DFT) Calculations**

Density functional theory (DFT)[23,24] calculations were performed using the Vienna *Ab-Initio* Simulation Package (VASP) code.[25,26] A plane wave cut-off energy of 400 eV and 3 × 3 × 1 Monkhorst-Pack[27] grid were used for total energy calculations. The interactions between the electrons and nuclei were treated with all electron like projector augmented wave (PAW) potentials with the generalized gradient approximation (GGA)[28,29] using PW91 functionals.[30] Ionic positions were optimized until Hellman-Feynman force on each ion was smaller than 0.02 eV/Å.

The Pt-terminated CoPt(111) surface was modeled using a four layer 3×3 surface slab. The Pt(111) surface was modified by replacing subsurface (2$^{nd}$ layer) Pt atoms with the Co atoms to model Pt-terminated CoPt(111) surface.[31] The mixed FeNi(111) surface was modeled using a four layer 4×4 surface slab. The Ni(111) surface was modified by replacing half of the Ni atoms in the top two layers with Fe atoms to model a mixed FeNi(111) surface to mimic the slab configuration for the previously reported FeNi-supported catalysts.[32] A vacuum layer of ~14 Å thick was added in the slab cell along the direction perpendicular to the surface in order to minimize the artificial interactions between the surface and its periodic images. During geometry optimization, atoms in the top two layers were allowed to relax while the atoms in the bottom two layers were fixed. The binding energy of an adsorbate is calculated as

$$BE(adsorbate) = E(slab+adsorbate) - E(slab) - E(adsorbate)$$

where E(slab+adsorbate), E(slab) and E(adsorbate) are the total energies of slab with adsorbate, clean slab and adsorbate species in gas phase, respectively. The detailed information regarding the mixed CoPt(111) and the Ni-terminated FeNi(111) can be found in the Supplementary Information.

## 3. Results and Discussion

### 3.1 Thermodynamic Analysis

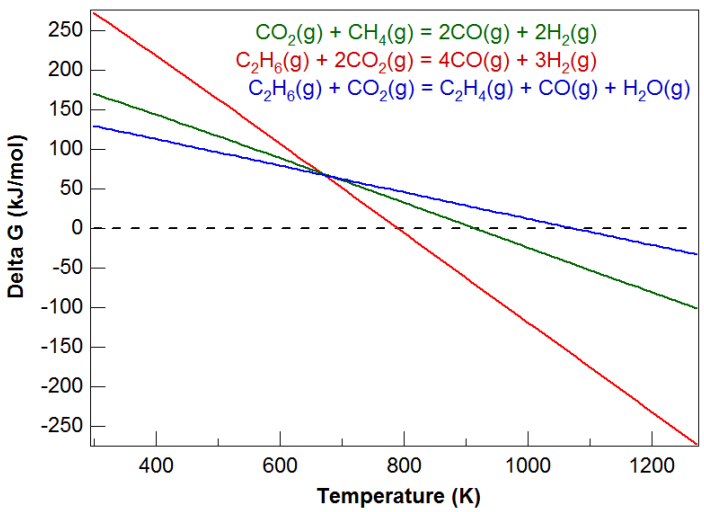


Figure 1. Thermodynamic analysis of dry reforming of methane (green) and ethane (red) and oxidative dehydrogenation of ethane with $CO_2$ (blue) using the HSC Chemistry 8 software.

A thermodynamic analysis to investigate the effect of temperature on the Gibbs free energy (ΔG) for DRM, DRE and ODEC from 298–1273 K is performed using the HSC Chemistry 8 software. As shown in Figure 1, temperature affects ΔG significantly: while all of the above reactions are highly endothermic at low temperature (298 K) due to the stable nature of the reactants, an increase in temperature to ~ 1173 K results in thermodynamically favorable for all three reactions. It should be pointed out that the temperature at which ΔG becomes zero varies significantly among the three reactions: the reaction temperature for DRE is lower by about 100 K and 200 K, compared to DRM and ODEC, respectively. This is in agreement with previous thermodynamic calculations by Xiaoding *et al.*[2] Lower reaction

temperature for DRE means less energy required and possibly reduced catalyst deactivation problems which are typically associated with coking and sintering resulted from high reaction temperatures. At sufficiently high temperatures, both DRE and ODEC occur simultaneously and hence it is important to identify catalysts which kinetically control the selectivity toward each reaction.

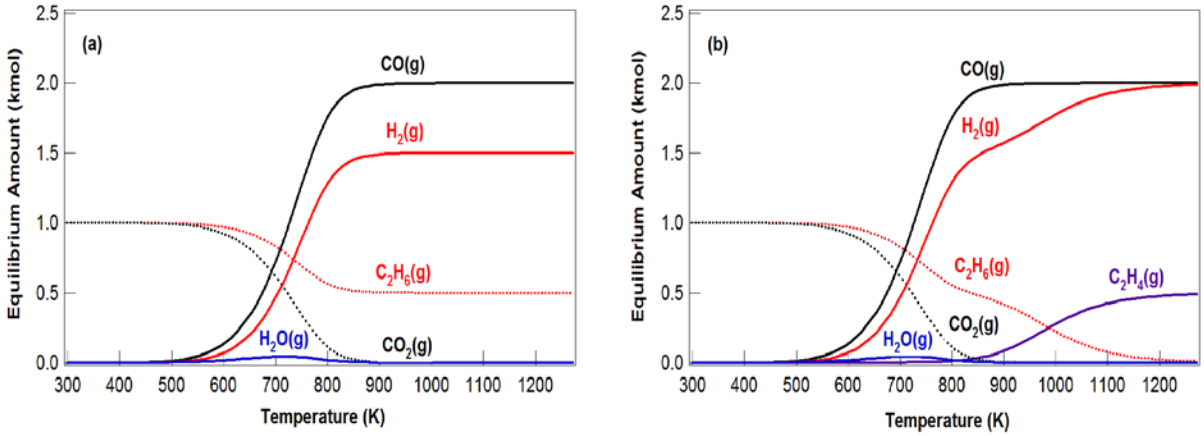


Figure 2. Thermodynamic equilibrium plots for $CO_2$ + $C_2H_6$ reaction at 1 atm from 373 – 1273 K and at inlet feed ratio of $CO_2$: $C_2H_6$ = 1 with products (a) CO, $H_2$ and $H_2O$ only (b) CO, $H_2$, $H_2O$ and $C_2H_4$. The plots were created by using Gibbs free energy minimization algorithm on HSC Chemistry 8 software.

Although industrial processes rarely operate at equilibrium, it has been shown that a variety of reforming catalysts can achieve compositions close to equilibrium.[1,33] Hence, equilibrium plots provide insights for thermodynamic limitations and the effects of variables such as temperature and pressure.[33] Noureldin *et al.*[33] established thermodynamic trends for syngas production from the reforming of natural gas using thermodynamic equilibrium modeling in order to maximize hydrogen generation and economic benefits. Parkhare *et al.*[34] studied the equilibrium compositions for the DRE process using the HSC Chemistry 7.1 software to identify the effect of reaction temperature. In this study, Gibbs free energy minimization simulation from the HSC Chemistry 8 software is used to generate thermodynamic equilibrium plots for the reactions of $CO_2$ and ethane at an equimolar ratio. Figure 2a shows the equilibrium concentrations of the $CO_2$ + ethane reaction with products CO, $H_2$ and $H_2O$ from 373 – 1273 K at 1 atm. The analysis indicates that the temperature affects equilibrium compositions significantly, particularly those of $H_2$ and

CO. The ratio of $H_2$ to CO, an important variable for syngas generation, progressively increases starting at 473 K and reaches 0.75 at 853 K, as expected from the reaction stoichiometry. The $H_2$/CO ratio then remains constant at 0.75 till 1273 K. Furthermore at 853 K, the ethane/$CO_2$ ratio approaches 0.5, consistent with the stoichiometric coefficients for DRE.

When simultaneous oxidative dehydrogenation reaction is considered, however, a different equilibrium composition is observed in Figure 2b after 823 K, where the production of ethylene begins. The ratio of $H_2$ to CO increases and eventually approaches unity at 1273 K, consistent with stoichiometry for ODEC. Figure 2b also shows a higher ethane conversion at high temperature. Based on trends in Figures 1, 2a and 2b, a reaction temperature of 873 K is selected to avoid gas phase reactivity and rapid catalyst deactivation associated with high reaction temperatures in order to investigate the catalytic activity of supported bimetallic catalysts in a flow reactor at steady-state. It should be pointed out that the equilibrium amounts in Figure 2b are calculated based on the assumption that all possible reactions, ODEC and DRE, are simultaneously taking place. Hence, while the reaction temperature of 873 K in Figure 2b results in a low equilibrium amount for ethylene, if ODEC alone is assumed to take place, by 873 K, ethane conversion to produce ethylene is achieved up to 20 %.

### 3.2 Catalyst Selection and Characterization

CoPt/$CeO_2$ has previously been identified as an active and selective catalyst for the catalytic reduction of $CO_2$ by hydrogen.[4] Compared to other bimetallic catalysts such as NiPt/$CeO_2$ and NiPd/$CeO_2$, CoPt/$CeO_2$ produces the highest amount of the desirable product CO, instead of fully reducing $CO_2$ into $CH_4$.[4] The combination of a reducible $CeO_2$ support with the active and selective CoPt bimetallic catalysts makes CoPt/$CeO_2$ a promising candidate for the reaction of $CO_2$ with ethane. However, in order to overcome the dependence for expensive and scarce precious metals, several non-precious metal bimetallic catalysts are selected for this study. Particularly, the activities of CoMo/$CeO_2$ catalyst, which replaces Pt with Mo, as well as NiMo/$CeO_2$, which employs Ni, the most common reforming transition metal, are investigated and compared with that of CoPt/$CeO_2$. Furthermore, since Fe is known to enhance the catalytic activity of Cr-supported catalysts in ODEC,[17] FeNi/$CeO_2$ is also studied in this work.

### 3.2.1 CO Uptake and Chemisorption

In order to obtain a quantitative comparison of the number of active sites on different catalysts via the amount of adsorbed CO, pulse CO chemisorption was performed. As shown in Table 1, the CO uptake values show the following trends: (1) $CoPt/CeO_2$ > $Pt/CeO_2$ > $Co/CeO_2$, (2) $Co/CeO_2$ > $Mo/CeO_2$ > $CoMo/CeO_2$, (3) $NiMo/CeO_2$ > $Ni/CeO_2$ > $Mo/CeO_2$, and (4) $FeNi/CeO_2$ > $Fe/CeO_2$ > $Ni/CeO_2$. In general, all bimetallic catalysts, except $CoMo/CeO_2$, have higher CO uptake values than those of the respective monometallic catalysts.

### 3.2.2 Temperature Programmed Reduction (TPR)

The reducibility of active metals in supported catalysts is investigated using temperature programmed reduction (TPR) and the comparison of each bimetallic catalyst with respective monometallic catalysts is shown in Figures 3a, 3b, 3c and 3d for $CoPt/CeO_2$, $CoMo/CeO_2$, $NiMo/CeO_2$ and $FeNi/CeO_2$, respectively. Generally, the TPR profiles of bimetallic catalysts are different from those of monometallic catalysts, suggesting that the formation of bimetallic bonds affects the reduction kinetics. Figure 3a shows that the reduction peaks of $CoPt/CeO_2$ shift to lower temperatures, compared to those of monometallic catalysts, indicating an increase in reducibility. As shown in Table 1, the bimetallic $CoPt/CeO_2$ catalyst shows a higher CO uptake value than the corresponding monometallic catalysts. This is likely due to the synergistic interaction between the two metals. The presence of Pt facilitates the dissociation of molecular hydrogen, which in turn promotes the reduction of $CoO_x$ species, leading to a higher dispersion of active metals and correspondingly a higher CO uptake value. However, the TPR profiles of $CoMo/CeO_2$ and $NiMo/CeO_2$ show a different trend. While the reduction peaks of both Co- and Ni-modified molybdenum bimetallic catalysts have higher reduction temperatures, compared to those of either Co or Ni alone, the bimetallic catalysts show lower reduction peak temperatures compared to the parent $Mo/CeO_2$ catalyst. This suggests that by modifying Mo with either Co or Ni, the reducibility of Mo is enhanced. In the case of $FeNi/CeO_2$, while the bimetallic catalyst shows a very similar TPR profile as $Fe/CeO_2$ with similar reduction temperatures, $FeNi/CeO_2$ clearly has a higher peak area, compared to the parent catalysts,

suggesting an increased reducibility. Overall, results in Figure 3 show a general increase in reducibility of active metals upon bimetallic formation.

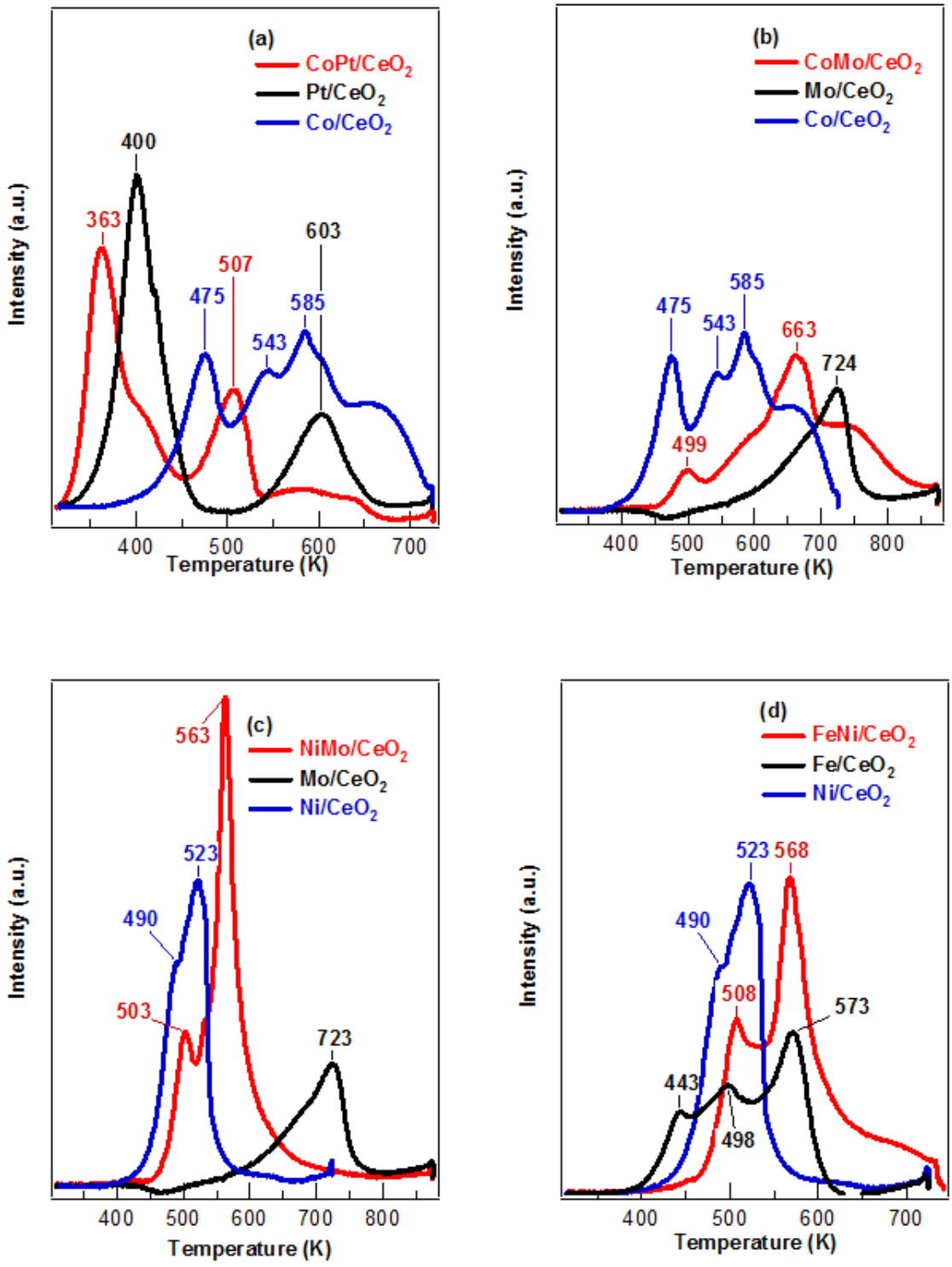

Figure 3. TPR profiles for comparison of bimetallic catalysts with respective monometallic catalysts (a) $CoPt/CeO_2$, $Pt/CeO_2$, $Co/CeO_2$, (b) $CoMo/CeO_2$, $Mo/CeO_2$, $Co/CeO_2$, (c) $NiMo/CeO_2$, $Mo/CeO_2$, $Ni/CeO_2$, and (d) $FeNi/CeO_2$, $Fe/CeO_2$, $Ni/CeO_2$.

### 3.3 Catalytic Evaluation

#### 3.3.1 Comparison of Bimetallic Catalysts

Table 1. summarizes the activity and selectivity of $CoPt/CeO_2$, $NiMo/CeO_2$, $CoMo/CeO_2$, $FeNi/CeO_2$ and the corresponding monometallic catalysts at 873 K. ~~Figures 4a, and 4b show the conversion (%), and selectivity (%), respectively.~~ Concentrations of carbon-containing products between 0 – 10 h on stream as a function of time on stream are shown in Figures 4 and 5 for bimetallic and monometallic catalysts, respectively.

**Table 1. Summary of flow reactor results for $CO_2$ + Ethane reaction (10 mL/min each) at 873 K diluted in 20 mL/min He. Values of conversion and selectivity calculated by averaging data points between 500 – 700 min on stream**

| Catalyst* | Chemisorption (μmol CO/g) | Conversion (%) | | Space-time Yield (* $10^{-5}$ $mol_{product}$ $g_{cat}^{-1}$ $min^{-1}$ ) | | TOF ($min^{-1}$) | | Selectivity for Carbon-containing Products | | |
|---|---|---|---|---|---|---|---|---|---|---|
| | | $CO_2$ | $C_2H_6$ | $CO_2$ | $C_2H_4$ | $CO_2$ | $C_2H_6$ | CO | $CH_4$ | $C_2H_4$ |
| $CoPt/CeO_2$ | 33.6 | 44.7 | 24.0 | 200 | 1.2 | 18.5 | 9.9 | 98.7 | 0.6 | 0.7 |
| $CoMo/CeO_2$ | 7.9 | 14.0 | 7.0 | 60 | 1.3 | 24.7 | 12.3 | 98.0 | 0.1 | 1.9 |
| $NiMo/CeO_2$ | 18.0 | 37.3 | 19.5 | 200 | 0.6 | 28.9 | 15.1 | 99.5 | 0.1 | 0.4 |
| $FeNi/CeO_2$ | 28.9 | 10.8 | 9.1 | 20 | 10 | 5.2 | 4.4 | 68.7 | 0.3 | 31.0 |
| $Pt/CeO_2$ | 23.2 | 18.2 | 8.8 | 90 | 2.8 | 10.9 | 5.3 | 97.0 | 0.4 | 2.6 |
| $Co/CeO_2$ | 10.2 | 19.4 | 4.7 | 100 | 0.9 | 26.6 | 6.5 | 99.3 | 0.1 | 0.6 |
| $Mo/CeO_2$ | 9.5 | 5.7 | 5.1 | 8.6 | 3.2 | 8.3 | 7.4 | 74.0 | 1.0 | 25.0 |
| $Ni/CeO_2$ | 12.0 | 20.5 | 13.3 | 60 | 5.0 | 23.8 | 15.4 | 93.7 | 0.2 | 6.1 |
| $Fe/CeO_2$ | 17.2 | 12.0 | 11.1 | 9.3 | 3.5 | 9.7 | 9.0 | 76.0 | 1.2 | 22.8 |

*For bimetallic catalysts, the metal loading corresponds to a Co/Pt (Co/Mo, Ni/Mo or Fe/Ni) atomic ratio of 3 to 1. The metal loadings in monometallic catalysts are 1.7 wt%, 0.5 wt%, 0.8 wt%, 0.5 wt% and 0.5 wt% for $Pt/CeO_2$, $Co/CeO_2$, $Mo/CeO_2$, $Ni/CeO_2$, and $Fe/CeO_2$, respectively.

As summarized in Table 1, among the bimetallic catalysts, on the basis of the mass of the catalysts, $CoPt/CeO_2$ shows the highest conversions for $CO_2$ and ethane, 44.7 and 24.0%, respectively, – approximately over two-fold higher than those in the monometallic catalysts. Upon replacing Pt with Mo, however, the conversions are reduced as much as three times, suggesting that $CoMo/CeO_2$ is less active than $CoPt/CeO_2$. However, when Ni, instead of Co, is alloyed with Mo, conversions of $CO_2$ and ethane are comparable to those of the $CoPt/CeO_2$ catalyst, with 37.3 and 19.5% for $CO_2$ and ethane conversions, respectively. This is a particularly promising result since $NiMo/CeO_2$ is a precious metal free catalyst which can potentially reduce the need for precious metal catalysts for DRE. Table 1 shows that all three bimetallic catalysts, $CoPt/CeO_2$, $CoMo/CeO_2$, $NiMo/CeO_2$, show high selectivity of over 98% for the reforming product CO via the C–C bond cleavage.

When Fe is alloyed with Ni, on the other hand, despite relatively low conversions, the formation of ethylene is observed. The selectivity for ethylene is 30% for $FeNi/CeO_2$, suggesting that FeNi shows promising selectivity to the ODEC reaction via the C–H bond cleavage. For all bimetallic reforming catalysts, conversions of $CO_2$ and ethane are approximately 2:1 and for the dehydrogenation $FeNi/CeO_2$ catalyst, conversions are nearly 1:1, consistent with the reaction stoichiometric coefficients, discussed previously in equations (1) and (2), respectively.

The TOF values shown in Table 1, however, suggest a different trend due to varying CO uptake values. Among bimetallic catalysts, the TOF trend of $CO_2$ shows that $NiMo/CeO_2$ > $CoMo/CeO_2$ > $CoPt/CeO_2$ > $FeNi/CeO_2$, resulting from low CO uptake in molybdenum-based bimetallic catalysts.

### 3.3.2 Comparison of Bimetallic Catalysts with Corresponding Monometallic Catalysts

As shown in Table 1, the $CoPt/CeO_2$ catalyst shows the highest activity on the basis of mass, compared to its monometallic catalysts, $Pt/CeO_2$ and $Co/CeO_2$. The TOF values in Table 1, in contrast, show that $Co/CeO_2$ has the highest TOF due to its low CO uptake. Selectivity at similar conversions, although not included, shows that all $CoPt/CeO_2$, $Pt/CeO_2$ and $Co/CeO_2$ catalysts have over 97% selectivity for the reforming product CO, suggesting that all catalysts favor the reforming pathway via the C–C bond cleavage. In the case of the $CoMo/CeO_2$ bimetallic catalyst, both the activity and TOF show the same

trend: $Co/CeO_2$ > $CoMo/CeO_2$ > $Mo/CeO_2$. While both $Co/CeO_2$ and $CoMo/CeO_2$ lead to CO selectivity over 98%, $Mo/CeO_2$ shows approximately 25% for ethylene selectivity. This means that by modifying Mo with Co, the selectivity could be tuned from partially selective to dehydrogenation to highly selective toward the reforming pathway.

For $NiMo/CeO_2$, modification of Mo with Ni enhances the activity of the bimetallic catalyst compared to either parent metal catalyst. Similar to $CoMo/CeO_2$, $NiMo/CeO_2$ shows over 99% selectivity for the reforming pathway. This result suggests that a highly active and stable non-precious $NiMo/CeO_2$ catalyst can be used to replace the need for the precious metal $CoPt/CeO_2$ catalyst for the DRE reaction. When $Ni/CeO_2$ is modified to form $FeNi/CeO_2$, the bimetallic catalyst shows a promising selectivity toward the ODEC pathway to form ethylene with selectivity up to 30%. A comparison of results in Figures 4, and 5 also reveals differences in the stability of monometallic and bimetallic catalysts. Generally, the stability of all bimetallic catalysts is enhanced compared to the corresponding monometallic catalysts. To obtain quantitative deactivation, the percent deactivation between 1–10 h on stream for all catalysts is calculated and shown in Table 2. The deactivation is reduced from 48.7 % in $Pt/CeO_2$ to 10.4 % in $CoPt/CeO_2$, suggesting that the addition of Co increases the stability of the $Pt/CeO_2$ catalyst. The same stability effect of Co is observed upon modification of $Mo/CeO_2$ with Co; the deactivation of $CoMo/CeO_2$ is reduced to 25.0 % from 38.5 % in $Mo/CeO_2$. Table 2 also shows that the deactivation of $Ni/CeO_2$ is significant, up to 52.8, consistent with previous reports.[5] However, the stability of the $NiMo/CeO_2$ bimetallic catalyst is significantly enhanced, compared to either parent monometallic catalyst. In fact, the stability of non-precious $NiMo/CeO_2$ is comparable to that of precious $CoPt/CeO_2$. Similarly, an enhanced stability is also observed in $FeNi/CeO_2$.

**Table 2. The metal loading and percent deactivation of bimetallic and monometallic catalysts**

| Catalyst* | Metal loading (wt%) | % Deactivation |
|---|---|---|
| $CoPt/CeO_2$ | 1.7 % Pt, 1.5 % Co | 10.4 |
| $CoMo/CeO_2$ | 0.8 % Mo, 1.5 % Co | 25.0 |
| $NiMo/CeO_2$ | 0.8 % Mo, 1.5 % Ni | 15.0 |
| $FeNi/CeO_2$ | 0.5% Ni, 1.4 % Fe | 28.9 |
| $Pt/CeO_2$ | 1.7 | 48.7 |
| $Co/CeO_2$ | 0.5 | 26.1 |
| $Mo/CeO_2$ | 0.8 | 38.5 |
| $Ni/CeO_2$ | 0.5 | 52.8 |
| $Fe/CeO_2$ | 0.5 | 62.3 |

*For bimetallic catalysts, the metal loading corresponds to a Co/Pt (Co/Mo, Ni/Mo or Fe/Ni) atomic ratio of 3 to 1. Deactivation percentages are calculated between 100 min and 630 min on stream.

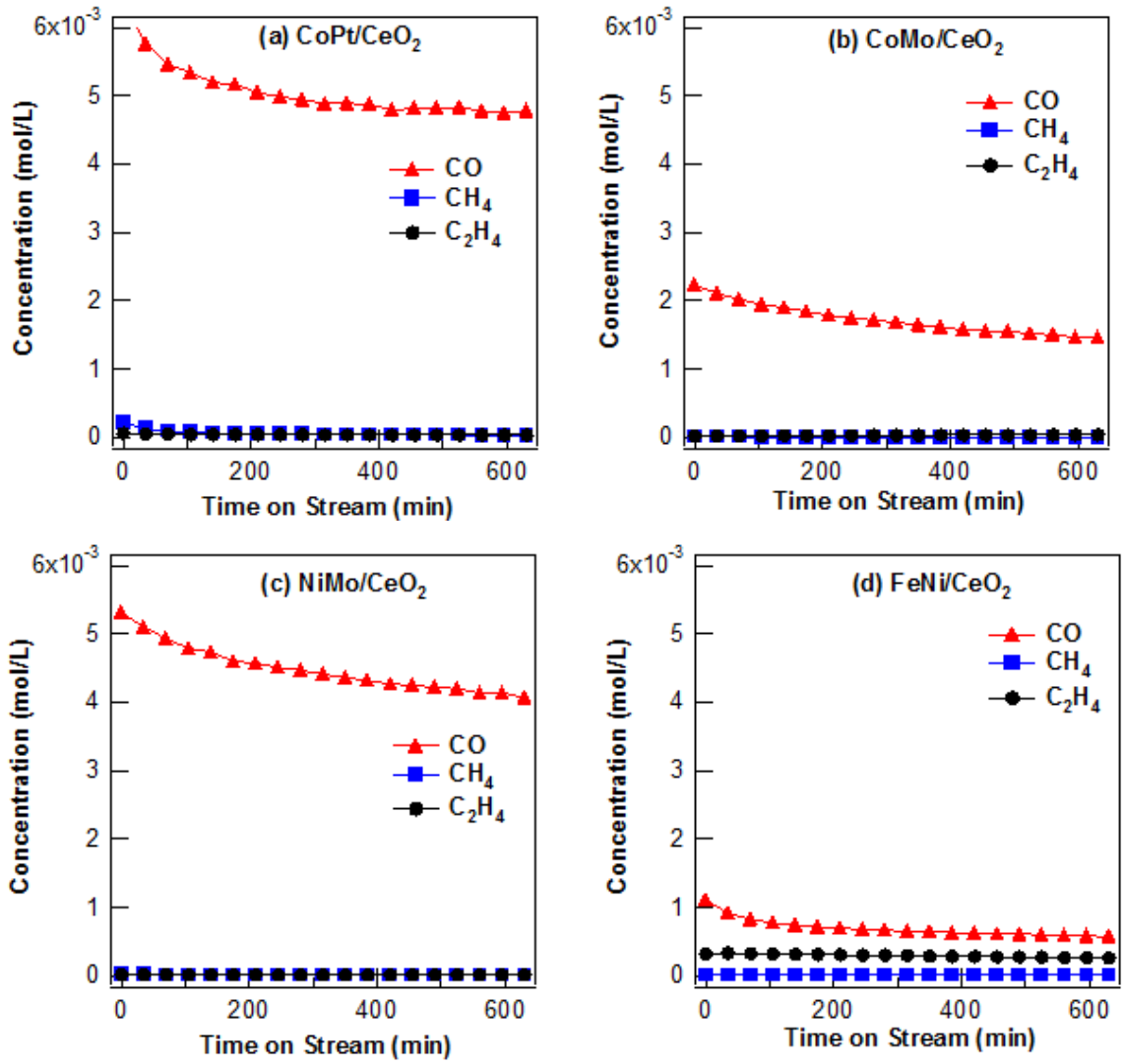


Figure 4. Concentration of carbon-containing products for reactions of ethane and $CO_2$ (10 mL/min each) diluted in 20 mL/min He at 873 K for (a) $CoPt/CeO_2$, (b) $CoMo/CeO_2$, (c) $NiMo/CeO_2$ and (d) $FeNi/CeO_2$ plotted versus time on stream.

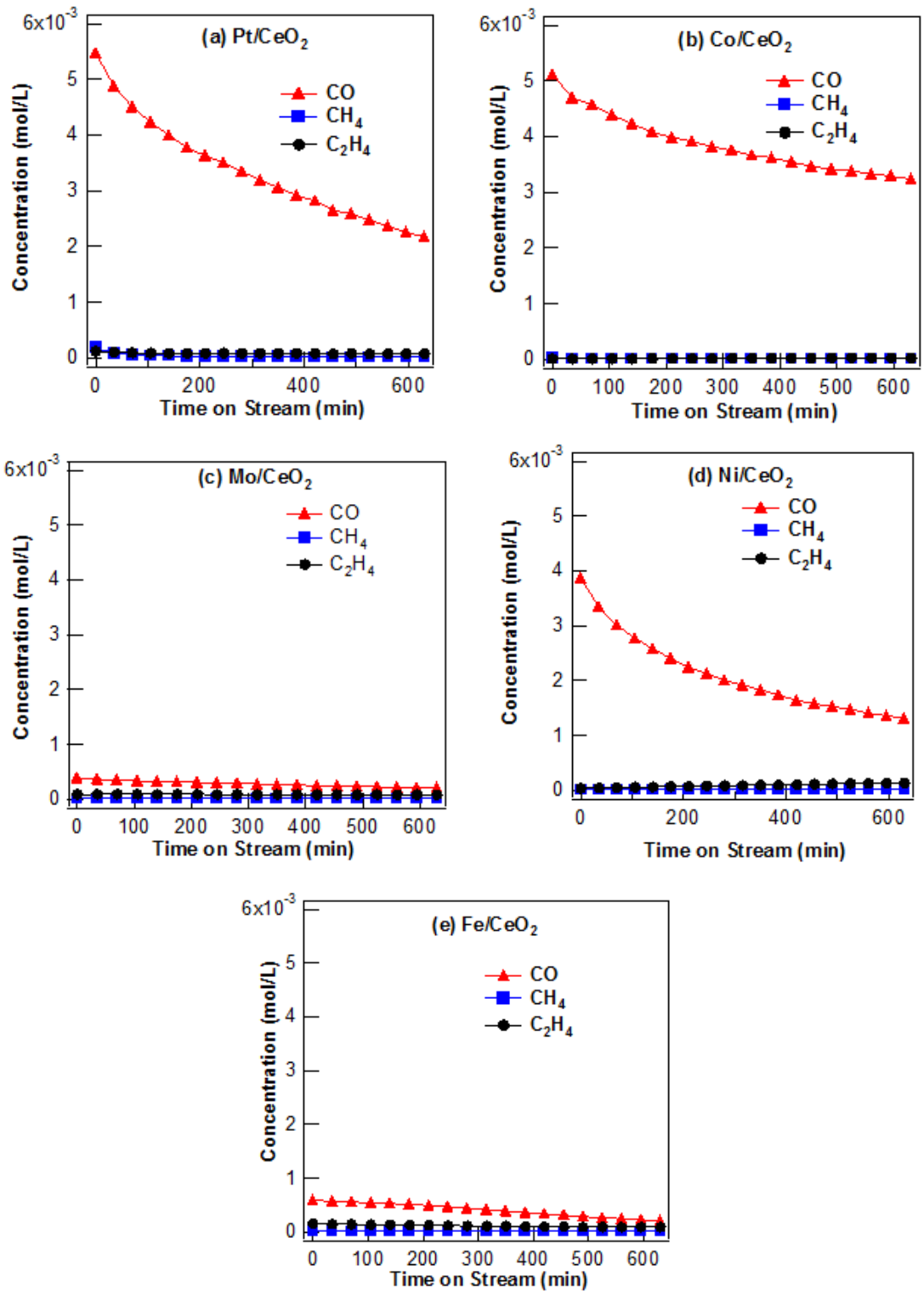


Figure 5. Concentration of carbon-containing products for reactions of ethane and $CO_2$ (10 mL/min each) diluted in 20 mL/min He at 873 K for (a) $Pt/CeO_2$, (b) $Co/CeO_2$, (c) $Mo/CeO_2$, (d) $Ni/CeO_2$ and (e) $Fe/CeO_2$ plotted versus time on stream.

### 3.4 Reaction Pathways via DFT Calculations

As summarized in the literature[31], the formation of bimetallic alloys modifies the surface d-band center and changes the binding energies of reactants and surface intermediates, leading to different catalytic activity and selectivity for several types of reactions. More detailed DFT calculations should be performed to identify general trends and descriptors for the reaction pathways of $CO_2$ with ethane. The CoPt and FeNi bimetallic systems are further investigated using DFT to gain more mechanistic insights for the DRE and ODEC pathways, respectively. As a simplified representation of the dominant plane of nanoparticles of CoPt and FeNi, model surfaces of CoPt(111) and FeNi(111) with the most thermodynamically stable facet are constructed without the $CeO_2$ support since recently we have reported that the calculated energy profiles for the reforming of ethane on Pt(111) and $CeO_2$/Pt(111) show a similar trend, although the strong metal-support interaction causes the reaction to be more thermodynamically favorable.[35] Based on previous studies, Pt-terminated CoPt(111),[31] Ni-terminated FeNi(111), mixed CoPt(111)[31] and mixed FeNi(111)[32] surface are selected to investigate the energy profile during the reaction. The binding energies of potential reaction intermediates for C–C and C–H bond cleavage for the reaction of ethane and $CO_2$ are calculated on the Pt-terminated CoPt(111) and mixed FeNi(111) surfaces shown in Figures 6a and 6b, respectively. The binding energies of potential reaction intermediates (Table S2) and the enthalpy change for the oxidative C–C and C–H bond cleavage of ethane (Figure S5) on CoPt(111) and FeNi(111) surfaces are calculated and provided in the Supplementary Information. In these calculations the surfaces are modified by oxygen atoms from the dissociation of $CO_2$. The results in Table 3 show that all intermediates bind more strongly on mixed FeNi(111) than on Pt-terminated CoPt(111). In addition, the results show that the binding energy difference between Pt-terminated CoPt(111) and the mixed surfaces is more pronounced for species adsorbed via the oxygen atom than those via the carbon atom (Figure 7) mainly because of significantly enhanced O binding on the mixed surfaces.

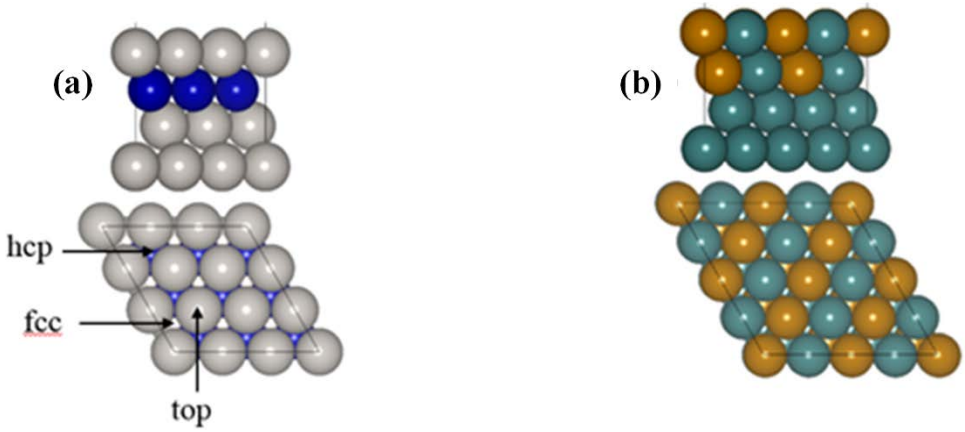


Figure 6. DFT optimized slabs models. Side (top) and top (bottom) views of (a) Pt-terminated CoPt(111) and (b) mixed FeNi(111) surfaces. Light grey: Pt, blue: Co, aqua: Ni and brown: Fe, respectively.

**Table 3. DFT calculated binding energies (in eV) of potential ethane dehydrogenation intermediates and atomic O on Pt-terminated CoPt(111) and mixed FeNi(111) surfaces.**

| Species | Pt-terminated CoPt(111) | | Mixed FeNi(111) | |
|---|---|---|---|---|
| | BE (eV) | site | BE (eV) | site |
| H | -2.40 | fcc | -2.87 | fcc(Fe, Fe, Ni) |
| O | -3.46 | fcc | -5.87 | fcc(Fe Fe, Ni) |
| CO | -1.10 | hcp | -1.84 | fcc(Fe, Ni, Ni) |
| $CH_3$ | -1.68 | top | -2.19 | fcc(Fe, Fe, Ni) |
| $CH_2CH_2$ | -0.37 | top-top | -0.94 | top(Fe)-hcp(Fe, Fe, Ni) |
| $CH_2CH$ | -2.00 | top-top | -2.96 | top(Fe)-hcp(Fe, Fe, Ni) |
| $CH_3CH_2$ | -1.51 | top | -1.82 | fcc(Fe, Fe, Ni) |
| $CH_3CH_2O$ | -1.43 | fcc | -3.17 | fcc(Fe, Fe, Ni) |
| $CH_3CHO$ | -0.24 | top | -0.65 | top(Fe)-fcc(Fe, Fe, Ni) |
| $CH_3CO$ | -1.84 | top | -2.31 | top(Fe)-fcc(Fe, Fe, Ni) |

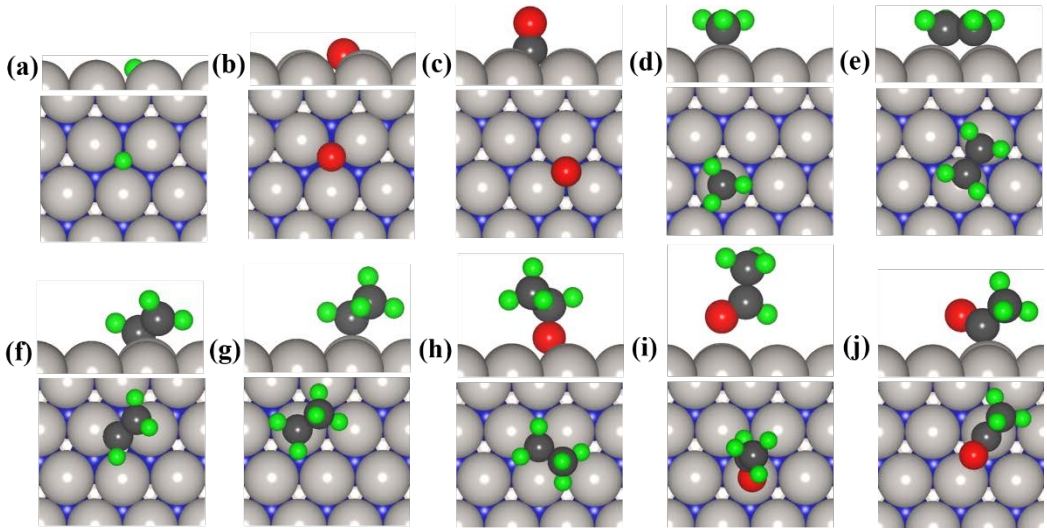


Figure 7. DFT calculated energetically most favorable binding configurations. Side (top) and top (bottom) views of (a) H, (b) O, (c) CO, (d) $CH_3$, (e) $CH_2CH_2$, (f) $CH_2CH$, (g) $CH_3CH_2$ (h) $CH_3CH_2O$, (i) $CH_3CHO$, and (j) $CH_3CO$ on the Pt-terminated CoPt(111) surface. Light grey: Pt, blue: Co, dark grey: C, red: O and green: H, respectively.

The change in energy for the oxidative C–C and C–H bond cleavage of ethane is calculated on all surfaces with two atomic oxygen preadsorbed on all surfaces. The energy profiles are shown in Figures 8a and 8b for the Pt-terminated CoPt(111) surface and the mixed FeNi(111) surfaces, respectively. Here the energy change is calculated for the reforming pathway via the C–C bond cleavage leading to products $CH_3$*, CO* and $H_2O$(g). For the oxidative dehydrogenation pathway, the energy change is calculated along a pathway via the C–H bond cleavage leading to products $CH_2CH$* and $H_2O$(g). For all surfaces, the atomic hydrogen is assumed to react with *O on the surface to form $H_2O$(g).

Figure 8a shows that on Pt-terminated CoPt(111), the C–C bond cleavage of ethane to form $CH_3$*, CO* and $H_2O$ (g) is exothermic, and energetically more favorable compared to the selective C–H bond scission to form $CH_2CH_2$*. In particular, it is found that the oxidation of ethane to form $CH_3CH_2O$* is energetically more favorable than the dehydrogenation of ethane to form $CH_3CH_2$*. The $CH_3CH_2O$* species subsequently undergoes two successive dehydrogenation reactions to form $CH_3CO$*, which then undergoes C–C bond cleavage to form $CH_3$* and CO*. Thus, the DFT results suggest that the Pt-terminated CoPt(111) surface promotes the reforming pathway to form CO. This is in agreement with the

flow reactor experimental studies shown in Table 1. Interestingly, however, the DFT calculated energy profile on the mixed CoPt(111) surface in Figure S5a does not show similar trend to that on the Pt-terminated CoPt(111) surface. Specifically, both the C–C and C–H bond scissions are endothermic and the energy difference between the two pathways is significantly reduced, as low as approximately 0.2 eV. This result implies that the mixed Co-Pt surface is neither selective to C–C bond scission nor C–H bond scission, which is different from the flow reactor results of selective C-C bond scission for reforming over the supported CoPt catalysts. This result suggests that CoPt/$CeO_2$ could be Pt-terminated under reaction conditions or experiments performed in the current study.

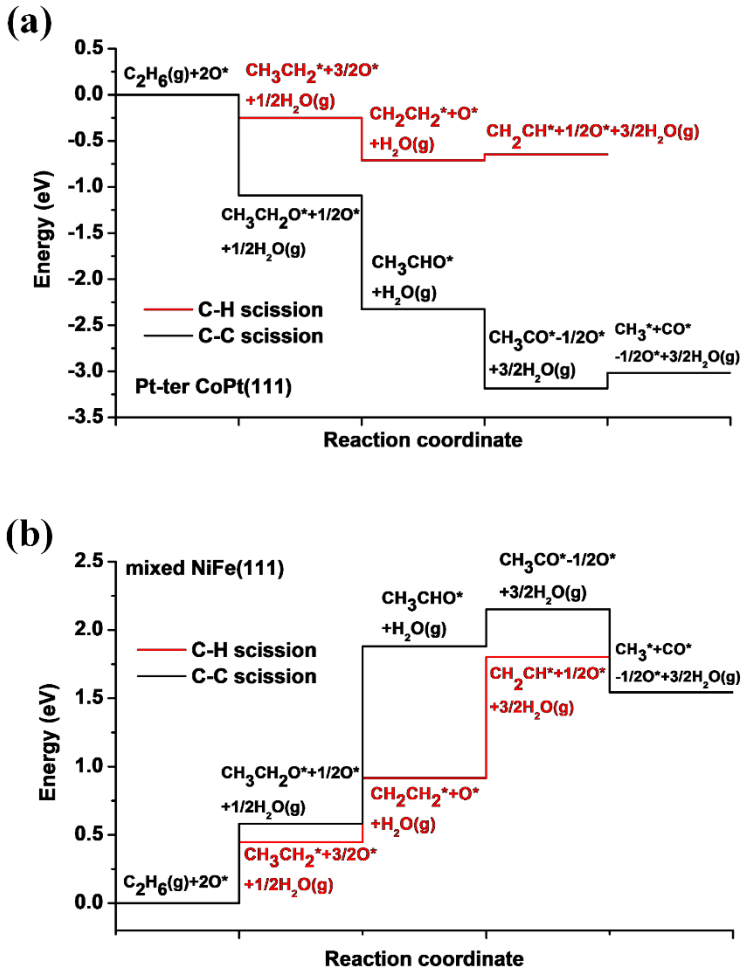


Figure 8. DFT calculated energy profile of reforming and oxidative dehydrogenation of ethane on (a) Pt-terminated CoPt(111) and (b) mixed FeNi(111).

In contrast to the Pt-terminated CoPt(111) surface, DFT calculations predict a different reaction scheme on the mixed FeNi(111) surface. On the mixed FeNi(111) surface, as shown in Figure 8b, the pathway for selective C–H bond cleavage (leading to product $CH_2CH_2$*) is energetically more favorable than the pathway for C–C bond cleavage. Thus the mixed FeNi(111) surface is predicted to preferentially dehydrogenate ethane to form $CH_2CH_2$. The DFT prediction supports the flow reactor data for the detection of ethylene as one of the major products over the FeNi/$CeO_2$ catalyst in Table 1. Instead, the energy profile on the Ni-terminated FeNi(111) surface in Figure S5b shows a reverse trend to the experimental data. On this surface, the oxidation of ethane to form $CH_3CH_2O$* is exothermic and energetically more favorable than the dehydrogenation of ethane to form $CH_3CH_2$*. Moreover, The C–C bond cleavage of ethane to form $CH_3$*, CO* and $H_2O$ (g) is energetically more favorable compared to the selective C–H bond scission to form $CH_2CH_2$*, which is highly endothermic. The DFT results suggest that the Ni-terminated FeNi(111) is quite selective to C–C bond scission to promote the reforming pathway. This result suggests that FeNi/$CeO_2$ could be mixed FeNi(111) under reaction conditions or experiments performed in the current study.

## 4. Conclusions

The catalytic performance of precious metal bimetallic catalyst, CoPt/$CeO_2$, and non-precious metal bimetallic catalysts, CoMo/$CeO_2$, NiMo/$CeO_2$, and FeNi/$CeO_2$ is compared for the reaction of $CO_2$ and ethane. In general the catalytic stability is enhanced in all bimetallic catalysts over the corresponding monometallic catalysts. In terms of selectivity, CoPt/$CeO_2$, CoMo/$CeO_2$, and NiMo/$CeO_2$ favor the reforming pathway to produce syngas via the C–C bond cleavage, while FeNi/$CeO_2$ shows promising selectivity to the oxidative dehydrogenation pathway to produce ethylene via the C–H bond cleavage. DFT calculated energy profiles on CoPt/$CeO_2$ and FeNi/$CeO_2$ confirm different reaction pathways, consistent with the experimental results.

## 5. Acknowledgements

The work was sponsored under Contract No. DE-AC02-98CH10886 with the U.S. Department of Energy, Office of Science. We acknowledge Dr. Shyam Kattel and Dr. Ping Liu for help in DFT calculations. We also acknowledge experimental assistance from Ms. Tianchi Ni and Mr. Brian McCarthy.

## 6. References


1. Noureldin, M. M. B.; Elbashir, N. O.; Gabriel, K. J.; El-Halwagi, M. M., *ACS Sustainable Chem. Eng.* **2015,** *3*, 625-636.
2. Xiaoding, X.; Moulijn, J. A., *Energy & Fuels* **1996,** *10*, 305-325.
3. Ansari, M. B.; Park, S.-E., *Energy Environ. Sci.* **2012,** *5*, 9419-9437.
4. Porosoff, M. D.; Chen, J. G., *J. Catal.* **2013,** *301*, 30-37.
5. Pakhare, D.; Spivey, J., *Chem. Soc. Rev.* **2014,** *43*, 7813-7837.
6. Theofanidis, S. A.; Galvita, V. V.; Poelman, H.; Marin, G. B., *ACS Catal.* **2015,** *5*, 3028-3039.
7. Edwards, J. H.; Maitra, A. M., *Fuel Processing Technology* **1995,** *42*, 269-289.
8. Brungs, A.; York, A. E.; Claridge, J.; Márquez-Alvarez, C.; Green, M. H., *Catalysis Letters* **2000,** *70*, 117-122.
9. Mimura, N.; Takahara, I.; Inaba, M.; Okamoto, M.; Murata, K., *Catal. Commun.* **2002,** *3*, 257-262.
10. Skoufa, Z.; Heracleous, E.; Lemonidou, A. A., *J. Catal.* **2015,** *322*, 118-129.
11. Shen, Z.; Liu, J.; Xu, H.; Yue, Y.; Hua, W.; Shen, W., *Appl. Catal., A* **2009,** *356*, 148-153.
12. Shi, X.; Ji, S.; Wang, K., *Catalysis Letters* **2008,** *125*, 331-339.
13. Schwab, E.; Milanov, A.; Schunk, S. A.; Behrens, A.; Schödel, N., *Chemie Ingenieur Technik* **2015,** *87*, 347-353.
14. Gärtner, C. A.; van Veen, A. C.; Lercher, J. A., *ChemCatChem* **2013,** *5*, 3196-3217.
15. Grubert, G.; Kondratenko, E.; Kolf, S.; Baerns, M.; van Geem, P.; Parton, R., *Catal. Today* **2003,** *81*, 337-345.
16. Wang, S.; Zhu, Z., *Energy & Fuels* **2004,** *18*, 1126-1139.
17. Deng, S.; Li, S.; Li, H.; Zhang, Y., *Ind. Eng. Chem. Res.* **2009,** *48*, 7561-7566.
18. Deng, S.; Li, H.; Li, S.; Zhang, Y., *J. Mol. Catal. A: Chem.* **2007,** *268*, 169-175.
19. Solymosi, F.; Németh, R., *Catalysis Letters* **1999,** *62*, 197-200.
20. Jin, L.; Reutenauer, J.; Opembe, N.; Lai, M.; Martenak, D. J.; Han, S.; Suib, S. L., *ChemCatChem* **2009,** *1*, 441-444.
21. Appel, L.; Eon, J.; Schmal, M., *Catalysis Letters* **1998,** *56*, 199-202.
22. Lonergan, W. W.; Vlachos, D. G.; Chen, J. G., *J. Catal.* **2010,** *271*, 239-250.
23. Hohenberg, P.; Kohn, W., *Physical review* **1964,** *136*, B864.
24. Kohn, W.; Sham, L. J., *Physical review* **1965,** *140*, 1133-&.
25. Kresse, G.; Furthmuller, J., *Phys. Rev. B: Condens. Matter Mater. Phys.* **1996,** *54*, 11169-11186.
26. Kresse, G.; Hafner, J., *Phys. Rev. B: Condens. Matter Mater. Phys.* **1993,** *48*, 13115-13118.
27. Monkhorst, H. J.; Pack, J. D., *Phys. Rev. B* **1976,** *13*, 5188.
28. Kresse, G.; Joubert, D., *Phys. Rev. B* **1999,** *59*, 1758.
29. Blöchl, P. E., *Phys. Rev. B* **1994,** *50*, 17953.
30. Perdew, J. P.; Wang, Y., *Phys. Rev. B* **1992,** *45*, 13244.
31. Yu, W.; Porosoff, M. D.; Chen, J. G., *Chem. Rev.* **2012,** *112*, 5780-5817.
32. Yu, W.; Xiong, K.; Ji, N.; Porosoff, M. D.; Chen, J. G., *J. Catal.* **2014,** *317*, 253-262.
33. Noureldin, M. M. B.; Elbashir, N. O.; El-Halwagi, M. M., *Ind. Eng. Chem. Res.* **2014,** *53*, 1841-1855.
34. Pakhare, D.; Shaw, C.; Haynes, D.; Shekhawat, D.; Spivey, J., *Journal of CO2 Utilization* **2013,** *1*, 37-42.
35. Porosoff, M. D.; Myint, M. N. Z.; Kattel, S.; Xie, Z.; Gomez, E.; Liu, P.; Chen, J. G., *Angew. Chem., Int. Ed.* **2015,** *54*, 15501-15505.